Supramolecular Coordination of Pb^{2+} Defects in Hybrid Lead Halide Perovskite Films Using Truxene Derivatives as Lewis Base Interlayers.

Ece Aktas[1,2,§], Jesús Jiménez-López[1,3,§], Cristina Rodríguez- Seco[1,3], Dr. Rajesh Pudi[1], Dr. Manuel A. Ortuño[1], Prof. Núria López[1] and Prof. Emilio Palomares[1–4,*]

1. Institute of Chemical Research of Catalonia-The Barcelona Institute of Science and Technology (ICIQ-BIST), Avda. Països Catalans 16, 43007 Tarragona, Spain
2. Department of Chemical Science and Technology, Avda. Països Catalans 16, 43007, Universitat Rovira i Virgili, 43007 Tarragona, Spain
3. Department d'Enginyeria Electrònica, Elèctrica i Automàtica, Univeristat Rovira i Virgili, Avda. Països Catalans 16, 43007 Tarragona, Spain
4. ICREA, Passeig Lluís Companys 23, 08010 Barcelona, Spain

§: Both authors contributed equally to this work.

*To whom the correspondence should be addressed: epalomares@iciq.es

Abstract.

Truxene derivatives, due to their molecular structure and properties, are good candidates for the passivation of defects when deposited onto hybrid lead halide perovskite thin films. Moreover, their semiconductor characteristics can be tailored through the modification of their chemical structure, which allows-upon light irradiation- the interfacial charge transfer between the perovskite film and the truxene molecules. In this work, we analysed the use of the molecules as surface passivation agents and their use in complete functional solar cells. We observed that these molecules reduce the non-radiative carrier recombination dynamics in the perovskite thin film through the supramolecular complex formation between the Truxene molecule and the Pb^{2+} defects at the perovskite surface. Interestingly, this supramolecular complexation neither affect the carrier recombination kinetics nor the carriers collection but induced noticeable hysteresis on the photocurrent *vs* voltage curves of the solar cells under 1 sun illumination.

INTRODUCTION.

The passivation of defects, in inorganic or hybrid photoactive thin films, results key to increase the solar cell efficiency[1–3]. The defects induce a change in the solar cell voltage reducing the energetic difference between the quasi-Fermi levels as a result of an increase carrier recombination and the solar cell photocurrent, because less photo-generated carriers are extracted[4–6].

In dye sensitized solar cells (DSSC), where mesoporous TiO_2 is used as scaffold to anchor dyes that act as light harvesters, the passivation of TiO_2 results key to achieve remarkable efficiencies[4,7,8]. For instance, the use of conformally deposited Al_2O_3 onto the nanocrystalline particles reduces the back-electron transfer to the oxidized dye but also decreases the number of defects on the TiO_2 nanocrystals surface, which act as carrier recombination centres[9].

Recently, in hybrid lead halide perovskite materials, many research groups have started to study the effect of molecules, as additives, to reduce the presence of surface defects [2,10,11]. As an example, the recent work of Di Carlo's group shows that the use of graphene oxide leads to an increase in the solar to energy conversion efficiency due to the suppression of carrier recombination centres associated to surface defects[12–14].

Organic molecules with truxene structure (see **Scheme 1, 1a**) have been explored[15] in organic solar cells[16–18], organic light emitting diodes[19], and as a hole transport material in perovskite solar cells[20–22] due to their good optical and semiconductor properties. In addition, truxene molecules have good solubility in most common organic solvents, which improves film morphology. Moreover, the truxene scaffold has an excellent thermal stability; a must when incorporated into organic electronic devices[23,24]. Their molecular structure and their molecular shape allow their deposition at the surface of the perovskite in face-to-surface configuration with strong interaction with the perovskite semiconductor surface. A similar approach has been observed for graphene oxide layers[25]. Furthermore, the introduction of 3-fluoropyridine substituents will act as a Lewis base to passivate the non-coordinated Pb^{2+} ions present at the surface of the perovskite.

In this work, we have synthesised a truxene derivative, 4,4',4''-(5,5,10,10,15,15-hexahexyl-10,15-dihydro-5H-diindeno[1,2-a:1',2'2-c]fluorine-2,7,12-triyl)tris(3-

fluoripyridine) (**Trux-FPy**), **Scheme 1**, and we have measured its optical and electronic properties. Moreover, we do have deposited a thin film of **Trux-FPy** on top of the methyl ammonium lead iodide (MAPI) hybrid perovskite and analysed its role as a Lewis base to passivate perovskite defects. Finally, we have measured the performance of complete MAPI perovskite solar cells and the effect of the **Trux-FPy** thin film as interfacial layer between the perovskite and the hole transport material (HTM) spiro-OMeTAD.

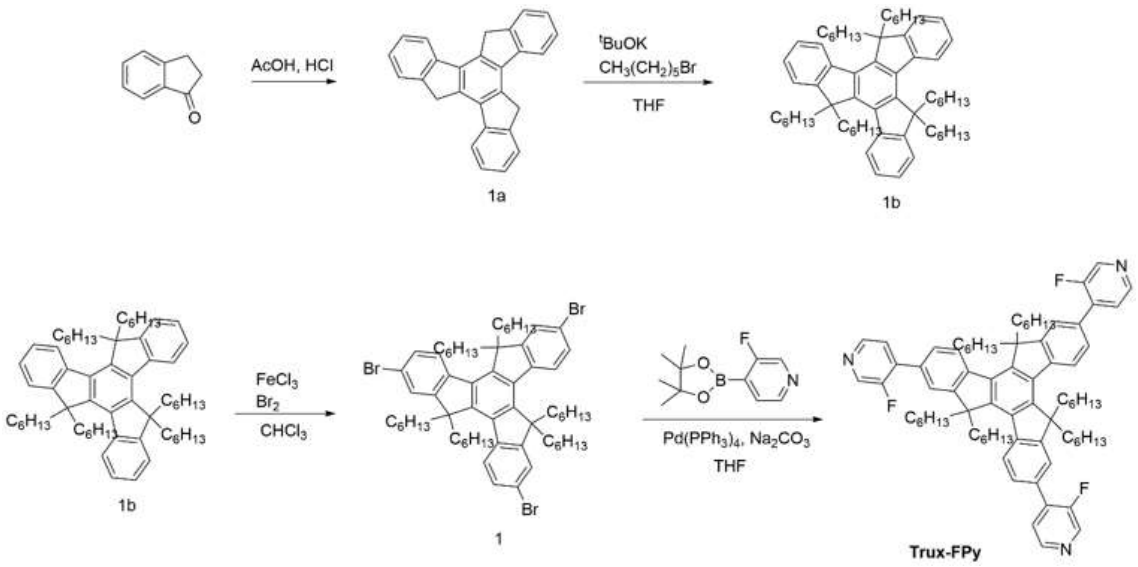

Scheme 1. Synthetic route for the **Trux-FPy**.

EXPERIMENTAL SECTION.

Synthesis of Trux-FPy.

The tetrahydrofuran (THF) used as the solvent for the synthesis of *1b*, and **Trux-FPy** was dried through standard procedure. The other reagents and solvents and used were purchased form Sigma-Aldrich© and TCl and used as received without further purification. The syntheses of *1a*, *1b*, and *1* was carried out following the scientific literature. Our ^{1}H and $^{13}C\{^{1}H\}$ NMR data was in good agreement with those values previously reported[18,26,27].

Synthesis of 10,15-dihydro-5*H*-diindeno(1,2-*a*;1',2'-*c*)fluorene (1a)

1-Indanone (0.5 g, 10.6 mmol) was dissolved in acetic acid (10.0 mL), and then concentrated hydrochloric acid (5.0 mL) was added. The solution was heated to 120 °C and refluxed overnight. The hot mixture was poured into saturated sodium carbonate aqueous solution (100.0 mL) with ice and stirred for 1 h. The yellow precipitate was filtered and washed with acetone (50.0 mL) and ethanol (50.0 mL) to give an off-white

powder **1a**. (0.8 g, 64% isolated yield). ^{1}H NMR (500 MHz, $CDCl_3$) δ 7.97 (d, *J* = 7.6 Hz, 3H), 7.71 (d, *J* = 7.4 Hz, 3H), 7.50 (t, *J* = 6.8, 3H), 7.40 (t, *J* = 7.4, 3H), 4.29 (s, 6H). ^{13}C{^{1}H} NMR (101 MHz, $CDCl_3$) δ 143.8, 141.7, 137.1, 135.3, 126.9, 126.3, 125.1, 121.9, 36.6.

Synthesis of 5,5,10,10,15,15-Hex(1-hexyl)10,15-dihydro-5*H*-diindeno(1,2-*a*;1',2'-*c*)fluorene (1b)

To a suspension of **1a** (0.5 g, 1.5 mmol) and ^{t}BuOK (5.7 g, 51.0 mmol) in dry THF (50.0 mL) 1-bromohexane (3.2 mL, 22.5 mmol) was added at room temperature under argon atmosphere. The resulting suspension was heated at 70 °C and stirred overnight. The solid material in the reaction mixture was removed through filtration and washed with hexane (100.0 mL). The filtrate part was concentrated down under reduced pressure and the resulting oil was dissolved in hexane (50.0 mL). The mixture was washed with 0.2 M HCl (25.0 mL) and saturated $NaHCO_3$ (50.0 mL). The organic layer was dried over $MgSO_4$ and concentrated *in vacuo*. Then, the residue was purified by silica column chromatography using hexane as eluent to afford the target compound **1b** as off-white powder (0.85 g, 67% isolated yield). ^{1}H NMR (400 MHz, $CDCl_3$)) δ 8.42 (d, *J* = 7.5 Hz, 3H), 7.54 – 7.48 (m, 3H), 7.46 – 7.35 (m, 6H), 3.19 – 2.89 (m, 6H), 2.27 – 1.98 (m, 6H), 1.09 – 0.78 (m, 36H), 0.64 (t, *J* = 7.1 Hz, 18H), 0.61 – 0.50 (m, 12H). ^{13}C{^{1}H} NMR (101 MHz, $CDCl_3$) δ 153.6, 144.8, 140.3, 138.4, 126.3, 125.9, 124.6, 122.1, 55.6, 37.0, 31.5, 29.5, 23.9, 22.3, 13.9.

Synthesis of 2,7,12-tribromo-5,5,10,10,15,15-hexahexyl-10,15-dihydro-5*H*-diindeno[1,2-*a*:1',2'-*c*]fluorene (1)

To a solution of compound **1b** (0.83 g, 0.98 mmol) in chloroform (8.0 mL) $FeCl_3$ (2.0 mg, 0.012 mmol) was added as catalyst. A solution of bromine (0.2 mL, 3.43 mmol) in chloroform (2.0 mL) was added dropwise under stirring at 0 °C. The mixture was allowed to warm to room temperature and stirred overnight. Then, a saturated Na_2SO_3 aqueous solution (20.0 mL) was added to remove excess bromine. The mixture was extracted with chloroform (3x50.0 mL), and the combined organic phases were dried over $MgSO_4$. After the solvent was removed, the yellow residue was recrystallized from ethanol to yield the compound **1** as an off-white powder (0.99 g, 93% isolated yield). ^{1}H NMR (400 MHz, $CDCl_3$) δ 8.17 (d, *J* = 8.5 Hz, 3H), 7.56 (d, *J* = 2.0 Hz, 3H), 7.51 (dd, *J* = 8.4, 2.0 Hz,

3H), 2.93 – 2.72 (m, 6H), 2.10 – 1.92 (m, 6H), 0.99 – 0.77 (m, 36H), 0.62 (t, J = 7.1 Hz, 18H), 0.51 – 0.36 (m, 12H). $^{13}C\{^{1}H\}$ NMR (101 MHz, $CDCl_3$) δ 155.9, 144.9, 138.9, 137.6, 129.4, 125.9, 125.5, 121.0, 56.0, 36.8, 31.4, 29.4, 23.9, 22.2, 13.9.

Synthesis of 4,4',4''-(5,5,10,10,15,15-hexahexyl-10,15-dihydro-5*H*-diindeno[1,2-*a*:1',2'-*c*]fluorene-2,7,12-triyl)tris(3-fluoropyridine) (Trux-FPy)

In a 50 mL two-neck round bottom flask **1** (0.25 g, 0.23 mmol), 3-fluoro-4-pyridine boronic acid pinacol ester (0.30 g, 1.38 mmol) and the system was purged with argon for 30 minutes. Then, freshly dried THF (15.0 mL) and Na_2CO_3 solution (2 M, 2.0 mL) were added to the medium. Finally, $Pd(PPh_3)_4$ (20.0 %, 53.0 mg) was added as catalyst and the reaction temperature was arranged to 80 °C and stirred for overnight. After that the solvent was removed *in vacuo*, chloroform ($CHCl_3$) (50.0 mL) was added to the crude product and the mixture was washed with brine (saturated) (2x50.0 mL) and water (2x50.0 mL) until a clear solution was obtained. The organic layer was dried over anhydrous $MgSO_4$, filtered and concentrated *in vacuo*. Finally, the residue was purified by silica column chromatography using Hexane:Ethyl acetate (2:1) as elution solvent. Precipitation from methanol yielded **Trux-FPy** as off-white powder (0.12 g, 46 % isolated yield). ^{1}H NMR (400 MHz, $CDCl_3$) δ 8.61 (d, J = 2.6 Hz, 3H), 8.54 (dd, J = 4.9, 0.8 Hz, 3H), 8.49 (d, J = 8.3 Hz, 3H), 7.76 (d, J = 1.7 Hz, 3H), 7.72 (d, J = 8.2 Hz, 3H), 7.58 (dd, J = 6.8, 5.0 Hz, 3H), 3.06 – 2.93 (m, 6H), 2.25 – 2.11 (m, 6H), 1.02 – 0.80 (m, 36H), 0.68 – 0.51 (m, 30H). $^{13}C\{^{1}H\}$ NMR (101 MHz, $CDCl_3$) δ 154.1, 146.4, 146.0, 141.2, 139.3, 139.0, 137.9, 136.2, 131.0, 127.0, 124.9, 124.1, 122.7, 56.0, 37.0, 31.4, 29.4, 24.0, 22.2, 13.8. Calcd for $C_{78}H_{96}F_3N_3^+$, (M^+): 1131.7551; found: 1131.7544 (0.6 ppm). Anal. Calcd for $C_{78}H_{96}F_3N_3$: C, 82.71; H, 8.54; N, 3.71. Found: C, 82.62; H, 9.00; N, 3.65.

Electrochemical measurements.

All electrochemical measurements were examined in a one-component cell under Nitrogen gas and equipped with a glassy-carbon working electrode, a platinum counter-electrode, and an Ag/Ag^+ reference electrode in acetonitrile solution at a concentration of 0.5 mM. The supporting electrolyte was a 0.1 M solution of tetrabutyl ammonium hexafluorophosphate ($TBAPF_6$). All potentials were corrected against Fc/Fc^+. The cyclic voltammogram (CV) was measured with a scan rate of 100 mV/s at room temperature.

UV-Visible absorption spectra.

UV-Vis measurements were carried out on an Agilent Cary 60 UV-Vis spectrophotometer equipped with two silicon diode detectors, double beam optics and Xenon pulse light.

Steady state fluorescence emission

Steady state fluorescence emission measurements were carried out on a Fluorolog Horiba Jobin Yvon spectrofluorimeter equipped with photomultiplier detector, double monochromator and Xenon light source.

Time correlated single photon counting measurements.

Lifetime measurements were carried out on a Edinburgh Instruments LifeSpec-II based on the time-correlated single photon counting (TCSPC) technique, equipped with a PMT detector, double subtractive monochromator and 470 nm picosecond pulsed diode lasers source.

Solar cells preparation.

FTO substrates are cleaned first with a cloth, brushing without damaging the FTO layer. Then, they are ultrasonicated with water and Hellmanex, isopropanol, and acetone, for 15 minutes for each one. Before depositing the TiO_2 layer, the substrates are treated with UV/Ozone for 15 minutes.

To deposit the compact TiO_2 layer, 40 µl of a 0.3 M $Ti(iPrO)_2(acac)_2$ solution in isopropyl alcohol (IPA) are spin coated at 4000 rpm for 25 s using an acceleration of 1000 rpm/s. Right after the spin coating process, the substrates are dried at 125 °C for 5 minutes. Then, they are transferred into a hot plate and calcined at 450^o C for 30 minutes.

Once the substrates are at room temperature, they are immersed in a 40 mM $TiCl_4$ solution at 70 °C for 30 minutes. Then, they are rinsed with water and ethanol consecutively and dried with a strong air flow.

Finally, a mesoporous TiO_2 layer is deposited. We used a commercially available 30 nm particle size TiO_2 paste (30NR-T, Dyesol) diluted in ethanol in a ratio 1:7 (w:w). 40 µl of this paste were spin coated at 6000 rpm for 30 s, using an acceleration of 1000 rpm.

The films are dried 5 minutes at 125 °C and after that they are calcined at 450 °C for 30 minutes. The substrates are then placed into a glovebox when they are still warm to avoid humidity.

The perovskite solution is prepared in a Nitrogen filled glove-box. In this case, we use $MAPbI_3$ perovskite. The concentration of the $MAPbI_3$ solution is 1.25 M. To prepare the solution, first, the required amount of PbI_2 is weighted and dissolved in DMSO. To help the solution of the lead salt, we heat up the solution to a temperature of 150 °C for 10 minutes. Then, the solution is cooled down to room temperature and the methyl ammonium iodide is added.

It is very important to control the atmosphere and the solvent vapours inside the glove-box. Hence, the work is carried out with a continuous N_2 flow that removes the dimethyl sulfoxide (DMSO) vapours.

The deposition of the perovskite solution is carried out using anti-solvent treatment. First, 40 μl of the perovskite solution are spin coated with a two-step programme. First, 1000 rpm for 10 s using an acceleration of 500 rpm, and then 4000 rpm for 30 s with an acceleration of 500 rpm. 10 seconds before the spinning process ends, 100 μl of chlorobenzene is spin coated right on the centre of the spinning substrate. The films are annealed for 45 minutes at 100 °C.

A 60 mM spiro-OMeTAD solution in chlorobenzene containing 38.7 μl/ml solution of tert-butylpyridine and 23.7 μl/ml solution of LiTFSI (stock solution 520 mg/ml in acetonitrile. The solution is stirred until spiro-OMeTAD is completely dissolved. Then, 30 μl are deposited dynamically by spin coating at 4000 rpm for 30 s.

For the substrates containing the **Trux-FPy** interlayer, 40 μl of a 5 mg/ml **Trux-FPy** solution in chlorobenzene are deposited at 4000 rpm for 30 s using an acceleration of 2000 rpm/s.

Then, the substrates are kept overnight in dry air and in the dark. Then, they are placed in the thermal evaporator and 80 nm of gold is evaporated on top as metal contact.

JV curves

The J-V curves were measured using a solar simulator (ABET 11000) and a source meter

(Keithley 2400). The curves were registered under 1 Sun conditions (100 mW/cm^2, AM 1.5G) calibrated with a Si-reference cell. The active area of the devices was 0.09 cm^2. The scan rate employed was 0.01 V/s. For the measurements with different light intensities, different optical filters were employed.

Photo-induced transient photovoltage, Transient photocurrent and charge extraction.

Photo-induced transient photovoltage (TPV), photo-induced transient photocurrent (TPC) and photo-induced charge extraction (CE) measurements were carried out using a white LED controlled by a programmable power supply and a control box that switches from open to short-circuit states. All the signals are recorded in an oscilloscope Yokogawa DLM2052 registering drops in voltage. Light perturbations pulses for TPV and TPC were provided by a nanosecond PTI GL-3300 nitrogen laser.

Electrostatic potential surface

The electrostatic potential surface was computed at Density Functional Theory on a model structure of **Trux-FPy**, where hexyl chains were replaced by methyl groups. The PBE density functional[28] was used together with Grimme's D3 dispersion scheme[29] as implemented in Gaussian 09[30]. The 6-31G** basis set was employed for all atoms[31,32], and diffuse functions were added to the electronegative F atoms[33]. The optimized structure and computational details can be consulted in the ioChem-BD repository[34,35].

RESULTS AND DISCUSSION.

The **Trux-FPy** show reversible oxidation and reduction processes (**Figure 1**). The oxidation waves of **Trux-FPy** were determined at +1.20 V and +0.95 V vs Ag/Ag$^+$ reference electrode in the oxidation process (**Figure 1**). Moreover, the **Trux-FPy** showed reversible reduction waves at -1.92 V and -1.85 V vs Ag/Ag$^+$ reference electrode.

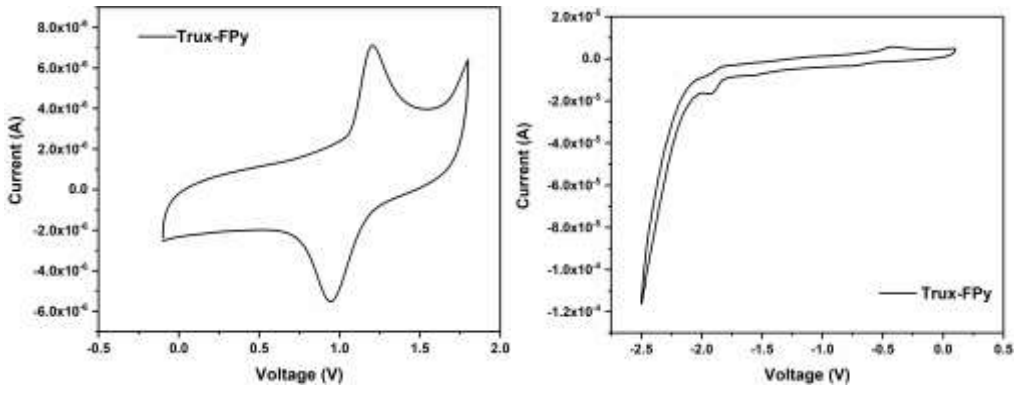

Figure 1. Single scan cyclic voltammogram of **Trux-FPy** on glassy-carbon electrode in 0.1 M TBAPF6/ACN solution. On the left the oxidation waves and on the right the reduction waves.

Using Fc/Fc^+ as internal reference electrode we have estimated the energies for the Highest Occupied Molecular Orbital (HOMO) and the Lowest Unoccupied Molecular Orbital (LUMO) energy levels[36]. The results are -5.37 eV and -2.42 eV, respectively. All the relevant electrochemical parameters are listed in **Table 1**.

Table 1: Summary of the most relevant parameters for the electrochemical measurements of **Trux-FPy**.

	$^{1/2}E_{ox1}$ (V)	$^{1/2}E_{ox2}$ (V)	$^{1/2}E_{red1}$ (V)	$^{1/2}E_{red2}$ (V)	HOMO (eV)	LUMO (eV)
Trux-FPy	1.20	0.95	1.92	1.85	**-5.37**	**-2.42**

Attending to the energy values given for the MAPI conduction band (CB) and valence band (VB) of -5.43eV and -3.90eV the **Trux-FPy** has a very low energy offset (E_{offset}) for the hole transfer, $E_{offset} = 0.07eV$. Such E_{offset} will suffice, as show later on, to allow carrier transport to the HTM, the spiro-OMeTAD.

Once the electrochemical characteristics of the **Trux-FPy** were measured, we turned onto the optical measurements. **Figure 2** illustrates the UV-Visible absorption spectra for the **Trux-FPy** in solution and in thin film.

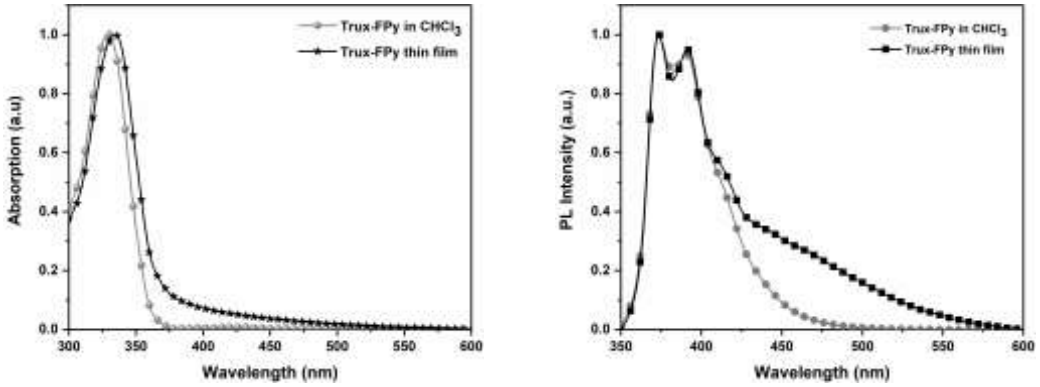

Figure 2. Left, normalized UV-Visible spectra (grey curve) for the Trux-FPy in chloroform ([Trux-FPy]=0.05 mM) and deposited in a cover slide glass (black curve) as

thin film (film thickness of 90 nm). Right, fluorescence emission spectra upon excitation at λ_{ex}= 340 nm measured at room temperature.

As can be seen in **Figure 2**, the **Trux-FPy** film does not show a noticeable new absorption band that may correspond to intermolecular interactions. Nonetheless, the main band in the UV region (λ_{max}= 340 nm) is slightly red shifted, which indicates the formation of molecular aggregates[37]. Notwithstanding the featureless UV-Visible spectra, the fluorescence emission spectra, on the contrary, shows remarkable fine structure with a visible shoulder centred λ_{em}=460 nm, which is in agreement with the presence of intermolecular interactions accounting for the existence of molecular aggregates.

The deposition of **Trux-FPy**, using the spin-coating technique, on top of a **MAPI** perovskite thin film shows modest quenching of the fluorescence emission (**Figure 3**), which indicates that due to the rather small E_{offset} between **MAPI** and **Trux-FPy** the interfacial hole transfer process is not efficient. Importantly, when **Trux-FPy** is used as an interfacial layer between **MAPI** and the HTM **spiro-OMeTAD,** the quenching process approaches unit yield, which implies outstanding interfacial charge transfer between the MAPI film and the HTM **spiro-OMeTAD** through the interfacial layer of **Trux-FPy**. It is important to highlight that the interfacial layer of **Trux-FPy** between **MAPI** and the HTM **spiro-OMeTAD** has a thickness of 5 nm approximately, which is thin enough to allow charge transport through it.

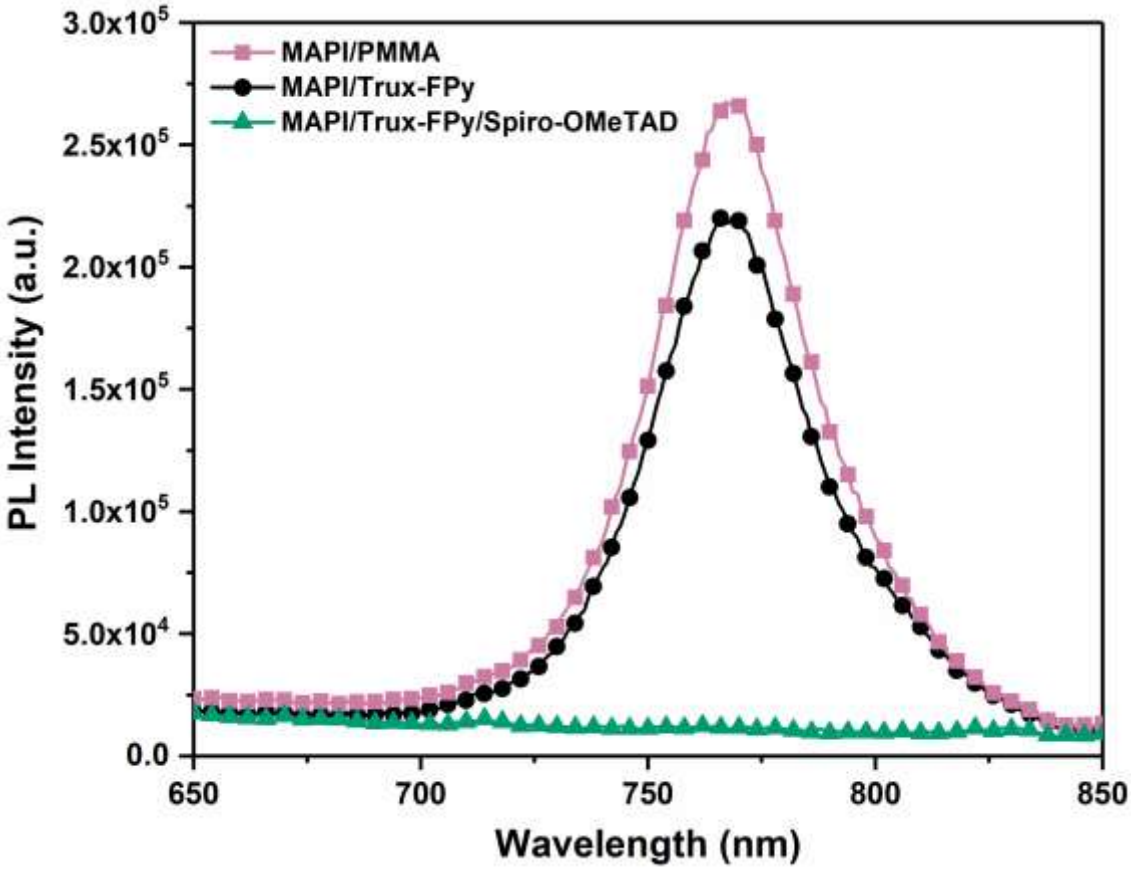

Figure 3. Luminescence emission band upon excitation at $\lambda_{ex=}$ 435 nm at room temperature for the MAPI/PMMA (total thickness of 450-500 nm), the MAPI/Trux-FPy (thickness ≃ 5 nm) and MAPI/Trux-FPy/spiro-OMeTAD (thickness = 150-200 nm)

Also, we focus in the role of **TruxFPy** in the passivation of the Lewis acid sites that act as traps for free carriers at the MAPI film surface, as we have previously hypothesised. **Figure 4** shows the luminescence emission decays recorded at room temperature, using the time correlated single photon-counting technique, using the same films as in **Figure 3**. Moreover, we have also added the **MAPI/spiro-OMeTAD** thin film for comparison purposes. The MAPI films were coated with PMMA with encapsulating purposes[38].

Time Resolved Photoluminescence (TRPL) decays show two different decay profiles. The faster decay is being assigned to trap filling whereas the slower decay corresponds to the bimolecular recombination[39–41]. TRPL decays are shown in **Figure 4** and they have been fitted to a biexponential decay, $y = A_1 \exp(-t/\tau_1) + A_2 \exp(t/\tau_2)$. The results of the fitting are shown in **Table 2**, obtaining a lifetime τ_1 = 69 ns and τ_1 = 53 ns for **MAPI/PMMA** and **MAPI/TruxFPy** samples, respectively. These kinetics, associated with trap filling, shows us the role of **TruxFPy**, passivating traps on the perovskite

surface, as it takes shorter times to be filled. It is also very interesting the analysis of the lifetime τ_2, which we already have assigned to bimolecular recombination in the perovskite. With values of 268 ns and 346 ns for **MAPI/PMMA** and **MAPI/TruxFPy**, it represents a direct evidence of the passivation effect of **TruxFPy** layer, indeed.

The passivation of Lewis acid sites at the surface of the **MAPI** perovskite leads to an improvement of the carrier's lifetime. This improvement is not seen, however, in the steady state luminescence emission represented in **Figure 2** as an increase in the perovskite emission quantum yield due to the effective but not efficient interfacial charge transfer between the **MAPI** film and the **Trux-FPy** film. Moreover, in good agreement with **Figure 2**, the luminesce decay for the sample **MAPI/Trux-FPy/spiro-OMeTAD** shows efficient quenching and much faster decay kinetics.

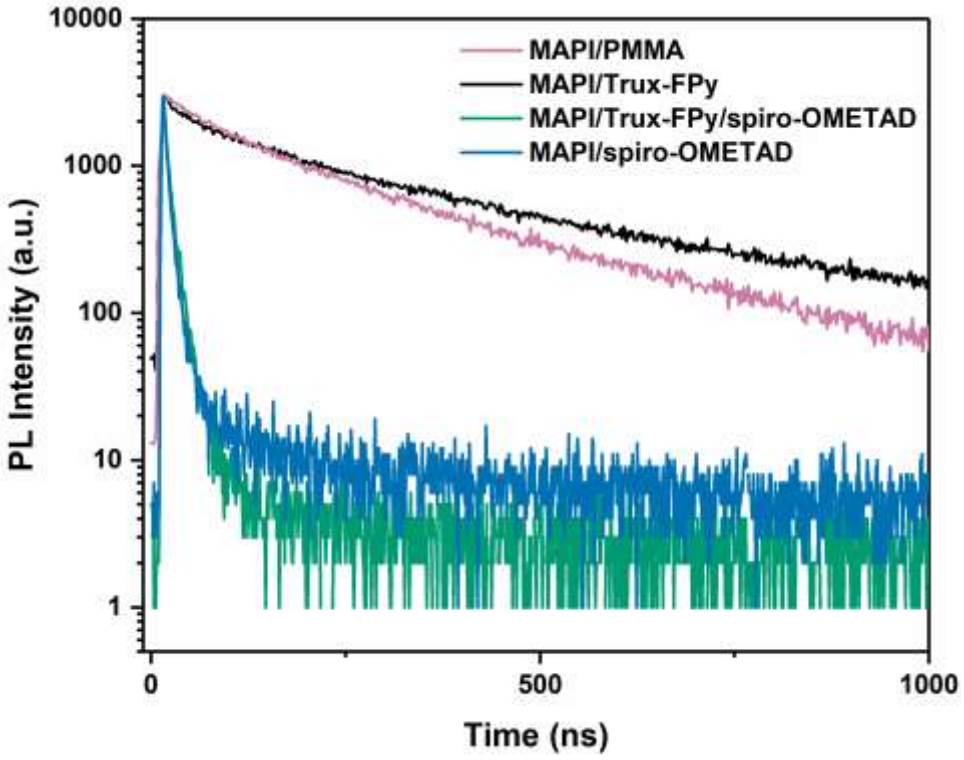

Figure 4. Normalized luminescence emission decays (λ_{ex}=470 nm) measured at room temperature for MAPI/PMMA, MAPI/spiro-OMETAD, MAPI/Trux-FPy, and MAPI/Trux-FPy/spiro-OMETAD on glass substrate.

Table 2. Fitting values obtained from the de-convolution of the luminescence decays in **Figure 4**.

Films	τ_1 (ns)	τ_2 (ns)
MAPI/PMMA	69	268
MAPI/spiro-OMETAD	5	21
MAPI/Trux-FPy	53	346
MAPI/Trux-FPy/spiro-OMETAD	5	16

We moved one-step further and fabricated solar cells to proof if the passivation of the surface defects using the **Trux-FPy** interfacial layer results also beneficial in a complete device.

Figure 5 illustrates the measured IV (photocurrent vs voltage) curves for the best **MAPI/Trux-FPy/spiro-OMeTAD** and the **MAPI/spiro-OMeTAD** used as a reference.

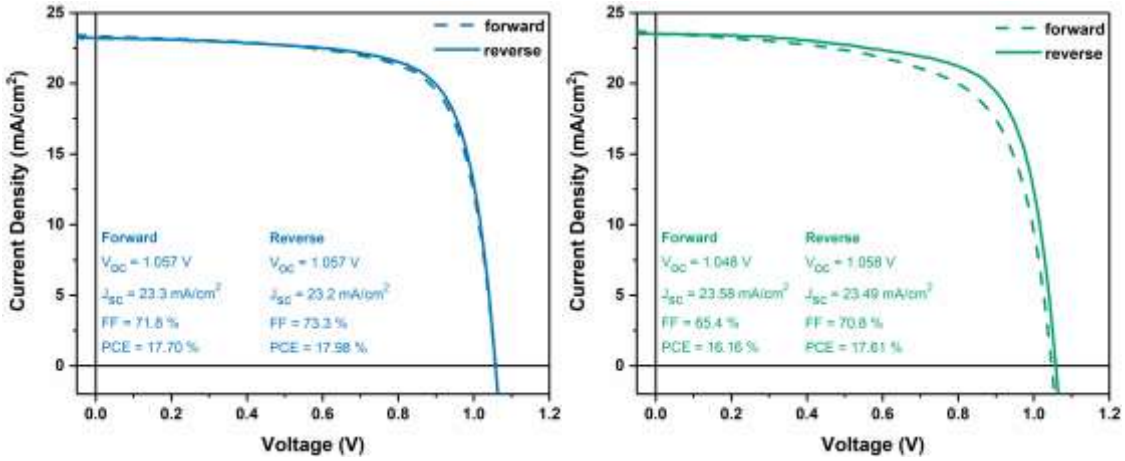

Figure 5. IV curves for the MAPI/spiro-OMeTAD (left, blue colour) and the MAPI/Trux-FPy/spiro-OMeTAD (right, green colour) solar cells when illuminated under sun simulated 1 sun conditions (100mW/cm^2 1.5 AM G).

At first glance, it is clear that the use of **Trux-FPy** as interfacial layer, although achieved the passivation of the **MAPI** surface as shown in **Figure 4**, does not improve noticeably the solar cell efficiency. A more detailed statistical study also supports this observation (**Figure 6**).

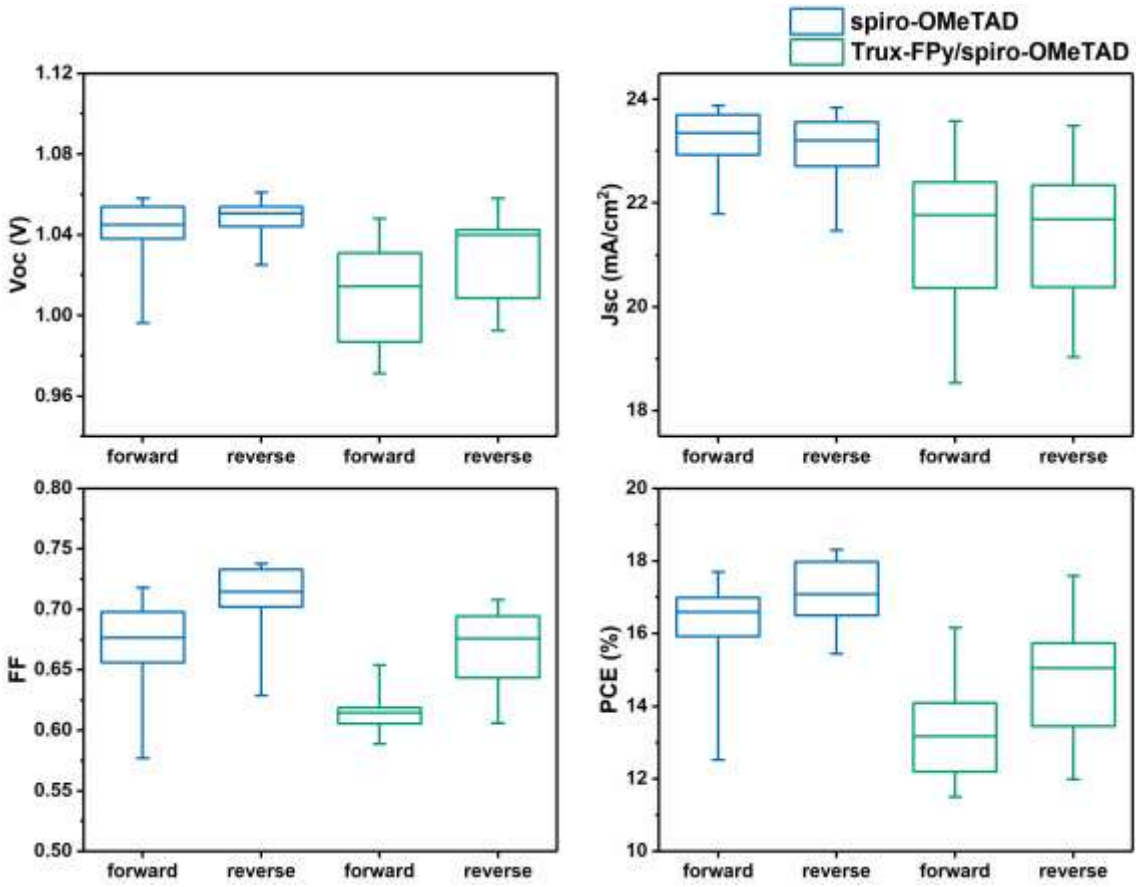

Figure 6. Statistics for different sets of devices employing MAPI/Trux-FPy/spiro-OMeTAD (green colour) and MAPI/spiro-OMeTAD (blue colour) sun simulated irradiated conditions at 1 sun.

We would like to highlight that even in the best case for the **MAPI/Trux-FPy/spiro-OMeTAD** solar cells there are minor differences between the forward (measured from short-circuit to open circuit) and the reverse (measured from open circuit to short circuit) IV curve. This difference accounts for the hysteresis process that has been largely discussed in the scientific literature for hybrid lead halide perovskites[42,43].

In this particular case the reference sample, measured under identical conditions, shows negligible hysteresis, which leads us to think that the observed differences are due to the presence of the **Trux-FPy** interlayer. A first hypothesis is that due to the low E_{offset} between the **MAPI** film and the **Trux-FPy** film, the latter results in a practical barrier that hampers the efficient transport of charges and will result in the accumulation of electronic holes and ionic species at the interface between the **MAPI** film and the **Trux-FPy** film. Hence, further studies, in complete devices under operando conditions, were carried out to analyse if the losses in efficiency were related to carrier losses due to

interfacial recombination processes. **Figure 7** illustrates the changes in open circuit voltage (V_{oc}) and short-circuit current upon illumination.

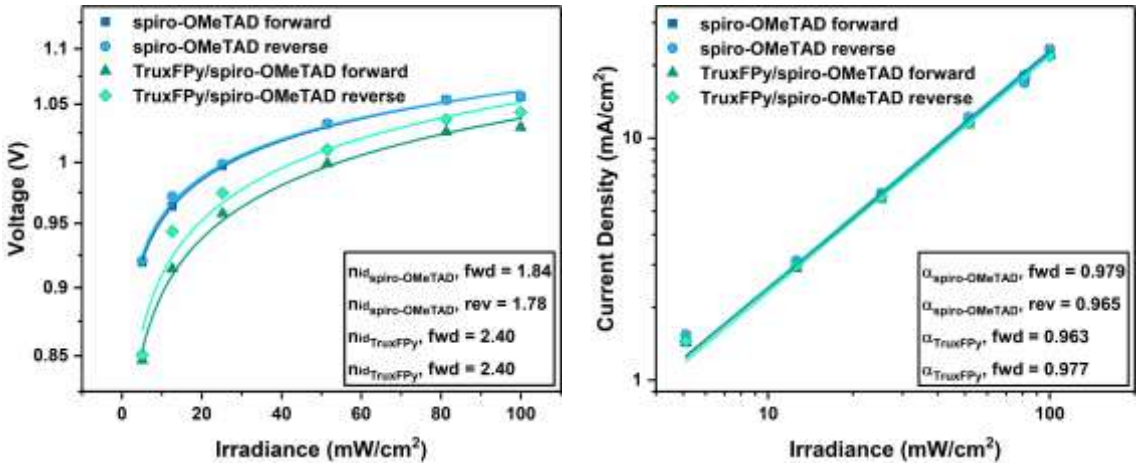

Figure 7. Left, V_{oc} *vs* light intensity and right, J_{sc} *vs* light intensity.

As can be seen in **Figure 7**, there is a substantial difference between the values for the **MAPI/Trux-FPy/spiro-OMeTAD** and the **MAPI/spiro-OMeTAD**. Those values correspond to the fitting of ***Equation 1***, where n is the ideality factor, *k* is the Boltzmann's constant, T is the temperature in Kelvin, q is the elementary charge and LI stands for light intensity.

Equation 1 $$Voc \propto n\frac{kT}{q}\ln(LI)$$

In non-ionic solar cells, values close to unity (*k*T/q) indicate that the bimolecular recombination is the dominant process. However, for values higher than 1 (1.7-1.8 for the **MAPI/spiro-OMeTAD** and 2.4 for **MAPI/Trux-FPy/spiro-OMeTAD**) it indicates that there are other parallel processes that occur during illumination. One of these is the reorganization of ions at the perovskite solar cell, which has been demonstrated to play a role in the final V_{oc} of the solar cell[44,45]. The major dependence of V_{oc} on irradiance and the higher slope value for **MAPI/Trux-FPy/spiro-OMeTAD** based perovskite solar cells implies that these processes have a greater impact when the **Trux-FPy** layer is present, which agrees with the greater hysteresis observed in **Figure 5.** Moreover, the analysis of the slope of the J_{sc} versus light illumination intensity gives similar values close to unity, which implies that carrier recombination at short circuit is negligible[46,47]. The JV curves measured to obtain these values are shown in **Figures S12** and **S13**.

We have shown previously that techniques such as photo-induced charge extraction (CE) and photo-induced transient photovoltage (TPV), developed to study DSSC (dye sensitized solar cells) and OSC (organic solar cells), can be very useful to understand carrier recombination and ion migration in perovskite solar cells. In this work, we do have used CE and TPV to measure the above mentioned solar cell properties. **Figure 8** shows the CE and TPV decays obtained under 1 sun illumination conditions for two of the best solar cells fabricated in this work.

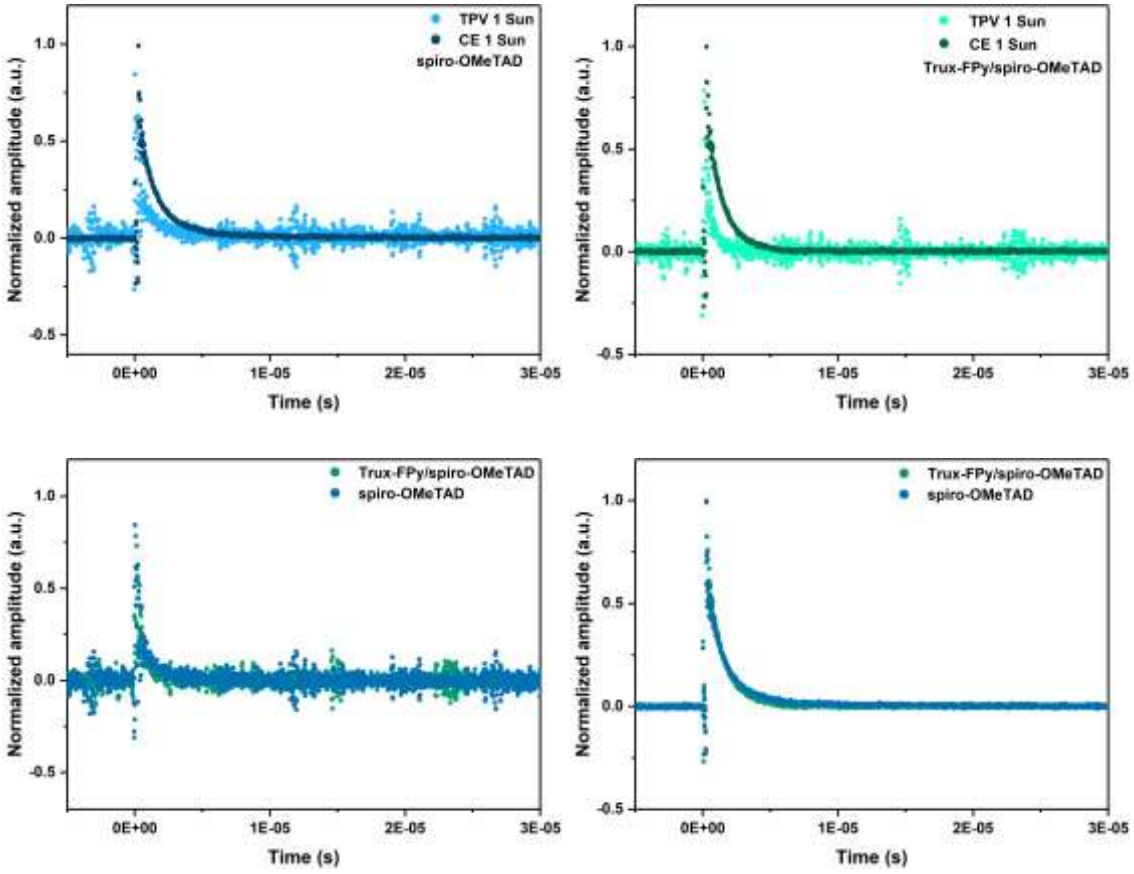

Figure 8. Top-left (spiro-OMeTAD), the decays at 1 sun for the CE and the TPV. Top-right (Trux-FPy/spiro-OMETAD) the decays at 1 sun for the CE and the TPV. Bottom-left, the normalized TPV decays comparison for both solar cells. Bottom-right, the normalized CE decays comparison for both solar cells.

As can be observed in **Figure 8**, in both perovskite solar cells the photo-induced carrier recombination at 1 sun measured using TPV and the charge extraction decays are very similar. Hence, we can conclude that the differences in the device performance are not due to the carrier recombination or the carrier extraction. To further confirm this

experimental observation, we measured the interfacial carrier recombination kinetics at different charge obtained at different light bias (different V_{oc} because of different light irradiation intensities) in **Figure 9**. In **Figures S14** and **S15** we show the dependence of carrier lifetime at different light bias and the carrier density at different light bias.

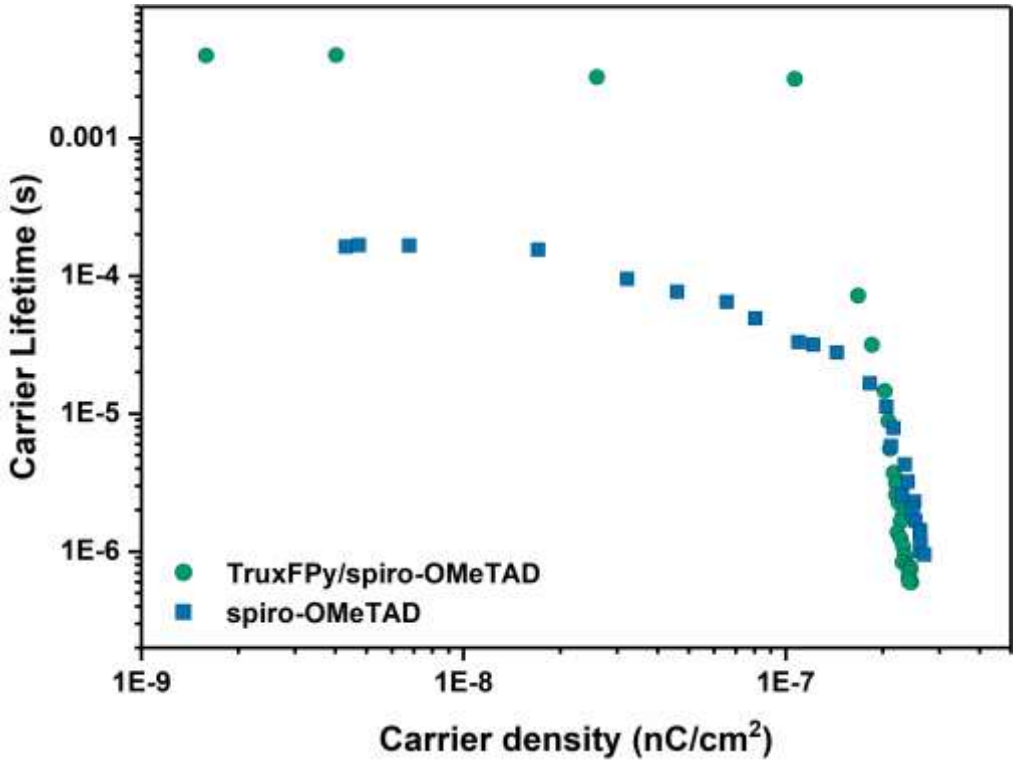

Figure 9. Carrier lifetime vs charge obtained for different light bias for MAPI/Trux-FPy/spiro-OMeTAD (green) and MAPI/spiro-OMeTAD (blue).

As illustrated in **Figure 9**, for charge values corresponding to light irradiation intensity close to 1 sun the carrier life time are alike and, moreover, the slope of the curves are also very close in units, which implies that the interfacial carrier recombination order is very much close. Thus, our first hypothesis that the possible accumulation of ions was responsible for the hysteresis resulted was incorrect. Nonetheless, taking into account the spectroscopic data, it results evident that the **Trux-FPy** do passivate the defects in the perovskite thin film.

We decided to focus more in depth on the Lewis base properties of the **Trux-FPy** and carried out a titration experiment using PbI_2 and the **Trux-FPy** molecule in solution. As can be seen in **Figure 10**, upon addition of increasing amounts of **Trux-FPy** an isosbestic

point appears at λ=350nm, which is indicative of a supramolecular interaction between the **Trux-FPy** and the Pb^{2+} ions. Moreover, the new supramolecular complex has a maximum absorption band at 325nm, which is 10nm blue shifted with respect to the **Trux-FPy** main absorption band in the UV.

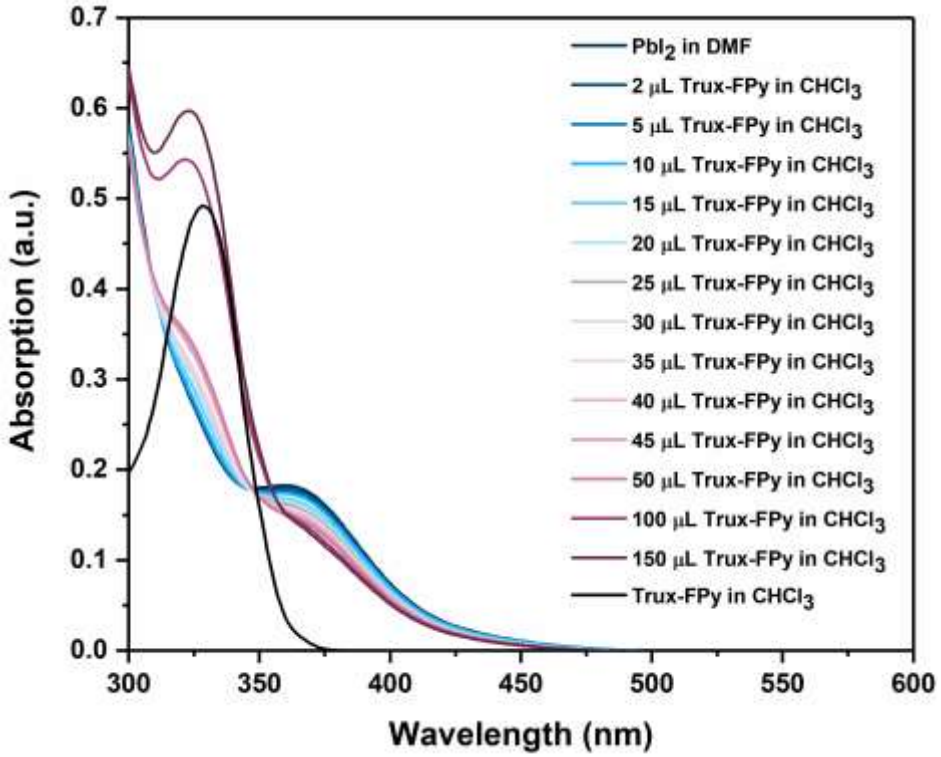

Figure 10. UV-Visible spectra of the titration experiment using 3mL of a 0.1 mM solution of PbI_2 in dimethylformamide (DMF) in a quartz cuvette and increasing concentration of Trux-FPy from a stock solution of 0.05 mM in chloroform.

Figure 11 shows the electrostatic potential (ESP) surface calculated at DFT level for a methyl derivative of **Trux-Fpy**. The molecule shows a planar π-conjugated core where the largest negative charges are localised on the pyridinic N atoms (density in red) and the F atoms (density in yellow). Hence, those N atoms are expected to coordinate the Pb^{2+} uncoordinated atoms at the perovskite surface through Lewis acid–Lewis base supramolecular interactions, which is in good agreement with the experiment shown in **Figure 10**.

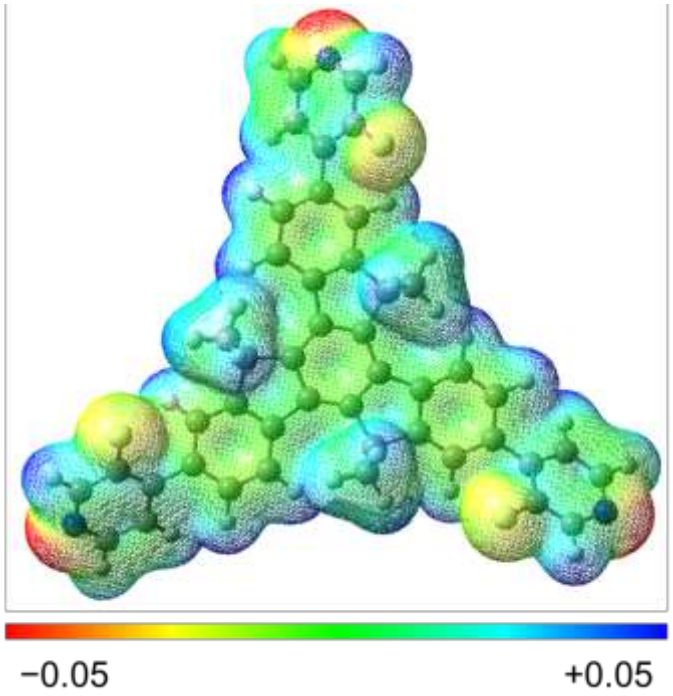

Figure 11. Electrostatic potential surface for a methylated model of the Trux-FPy molecule.

CONCLUSIONS.

We have designed and synthesised an organic semiconductor molecule with truxene core. The molecule, **Trux-FPy**, was intended to contain peripheral moieties that can work as Lewis bases to passivate surface defects in lead halide perovskite as a result of the non-coordinated lead contained in methyl ammonium lead iodide perovskite thin films. Those surface defects act as traps for carriers and increase the carrier recombination, which, in overall, limits the solar cell efficiency. The **Trux-FPy** was fully electrochemically and optically characterized and it was found that, upon deposition on top of the **MAPI** thin film, the **Trux-FPy** thin film decreases the number of defects at the **MAPI** surface increasing its luminescence lifetime. Moreover, the **Trux-FPy** thin film was capable of carrying out interfacial charge transfer processes with the **MAPI** thin film upon illumination, which leads us to incorporate the **Trux-FPy** as interfacial layer.

Once incorporated as an interfacial layer between the **MAPI** film and the HTM **spiro-OMeTAD** film, the best solar cells matched the efficiency of those standards prepared

using only **spiro-OMeTAD**. Nonetheless, the presence of hysteresis in the IV curves for the **Trux-FPy** containing solar cells was noticed.

An analysis in depth of the **MAPI/Trux-FPy/spiro-OMeTAD** solar cells using CE and TPV techniques determines that the interfacial carrier recombination processes in these devices are not affected by the presence of the **Trux-FPy** interfacial layer. Nevertheless, the **Trux-FPy** interfacial layer does have supramolecular interactions with the uncoordinated lead ions. Our results show the potential of surface supramolecular interactions between the perovskite semiconductor and intermediate layers to decrease the uncoordinated site defects, which are the cause negative effects in the perovskite solar cells performance.

Acknowledgements.

All the authors would like to acknowledge economic support from MICINN (project CTQ2016-80042-R) and Generalitat de Catalunya for the AGAUR funding (project 2017 SGR 00978). M.A.O. also acknowledges the "Juan de la Cierva–Incorporación" program (IJCI-2016-29762) for financial support. Prof. Palomares also thanks the reviewers for their critical review of the work, which indeed has been very useful.

Keywords: Lewis base, perovskite, solar energy, truxene

References.

[1] H. Tan, A. Jain, O. Voznyy, X. Lan, F. P. García de Arquer, J. Z. Fan, R. Quintero-Bermudez, M. Yuan, B. Zhang, Y. Zhao, et al., *Science* **2017**, *355*, 722–726.

[2] F. Wang, S. Bai, W. Tress, A. Hagfeldt, F. Gao, *npj Flex. Electron.* **2018**, *2*, 22.

[3] X. Zheng, B. Chen, J. Dai, Y. Fang, Y. Bai, Y. Lin, H. Wei, X. C. Zeng, J. Huang, *Nat. Energy* **2017**, *2*, 17102.

[4] N. Kopidakis, N. R. Neale, A. J. Frank, *J. Phys. Chem. B* **2006**, *110*, 12485–12489.

[5] F. Giordano, A. Abate, J. P. Correa Baena, M. Saliba, T. Matsui, S. H. Im, S. M. Zakeeruddin, M. K. Nazeeruddin, A. Hagfeldt, M. Graetzel, *Nat. Commun.* **2016**, *7*, 1–6.

[6] J. M. Ball, A. Petrozza, *Nat. Energy* **2016**, *1*, 16149.

[7] T. C. Li, M. S. Góes, F. Fabregat-Santiago, J. Bisquert, P. R. Bueno, C. Prasittichai, J. T. Hupp, T. J. Marks, *J. Phys. Chem. C* **2009**, *113*, 18385–18390.

[8] B. C. O'Regan, J. R. Durrant, P. M. Sommeling, N. J. Bakker, *J. Phys. Chem. C* **2007**, *111*, 14001–14010.

[9] E. Palomares, J. N. Clifford, S. A. Haque, T. Lutz, J. R. Durrant, *Chem. Commun.* **2002**, 1464–1465.

[10] C. M. Wolff, F. Zu, A. Paulke, L. P. Toro, N. Koch, D. Neher, *Adv. Mater.* **2017**, *29*, 1700159.

[11] D. Song, D. Wei, P. Cui, M. Li, Z. Duan, T. Wang, J. Ji, Y. Li, J. M. Mbengue, Y. Li, et al., *J. Mater. Chem. A* **2016**, *4*, 6091–6097.

[12] A. Agresti, S. Pescetelli, L. Cinà, D. Konios, G. Kakavelakis, E. Kymakis, A. Di Carlo, *Adv. Funct. Mater.* **2016**, *26*, 2686–2694.

[13] L. Najafi, B. Taheri, B. Martín-García, S. Bellani, D. Di Girolamo, A. Agresti, R. Oropesa-Nuñez, S. Pescetelli, L. Vesce, E. Calabrò, et al., *ACS Nano* **2018**, *12*, 10736–10754.

[14] A. Agresti, S. Pescetelli, B. Taheri, A. E. Del Rio Castillo, L. Cinà, F. Bonaccorso, A. Di Carlo, *ChemSusChem* **2016**, *9*, 2609–2619.

[15] F. Goubard, F. Dumur, *RSC Adv.* **2015**, *5*, 3521–3551.

[16] C. B. Nielsen, E. Voroshazi, S. Holliday, K. Cnops, B. P. Rand, I. McCulloch, *J. Mater. Chem. A* **2013**, *1*, 73–76.

[17] C. B. Nielsen, E. Voroshazi, S. Holliday, K. Cnops, D. Cheyns, I. McCulloch, *J. Mater. Chem. A* **2014**, *2*, 12348–12354.

[18] H. Tsuji, Y. Ota, S. Furukawa, C. Mitsui, Y. Sato, E. Nakamura, *Asian J. Org. Chem.* **2012**, *1*, 34–37.

[19] C. Yao, Y. Yu, X. Yang, H. Zhang, Z. Huang, X. Xu, G. Zhou, L. Yue, Z. Wu, *J. Mater. Chem. C* **2015**, *3*, 5783–5794.

[20] K.-H. Lin, A. Prlj, C. Corminboeuf, *J. Phys. Chem. C* **2017**, *121*, 21729–21739.

[21] F. J. Ramos, K. Rakstys, S. Kazim, M. Grätzel, M. K. Nazeeruddin, S. Ahmad, *RSC Adv.* **2015**, *5*, 53426–53432.

[22] K. Rakstys, A. Abate, M. I. Dar, P. Gao, V. Jankauskas, G. Jacopin, E. Kamarauskas, S. Kazim, S. Ahmad, M. Grätzel, et al., *J. Am. Chem. Soc.* **2015**, *137*, 16172–16178.

[23] M. Kimura, S. Kuwano, Y. Sawaki, H. Fujikawa, K. Noda, Y. Taga, K. Takagi, *J. Mater. Chem.* **2005**, *15*, 2393.

[24] J. Wang, Y. Chen, M. Liang, G. Ge, R. Zhou, Z. Sun, S. Xue, *Dye. Pigment.* **2015**, *125*, 399–406.

[25] H. Li, L. Tao, F. Huang, Q. Sun, X. Zhao, J. Han, Y. Shen, M. Wang, *ACS Appl. Mater. Interfaces* **2017**, *9*, 38967–38976.

[26] L. Liu, S. G. Telfer, *J. Am. Chem. Soc.* **2015**, *137*, 3901–3909.

[27] C. Huang, W. Fu, C. Z. Li, Z. Zhang, W. Qiu, M. Shi, P. Heremans, A. K. Y. Jen, H. Chen, *J. Am. Chem. Soc.* **2016**, *138*, 2528–2531.

[28] J. P. Perdew, K. Burke, M. Ernzerhof, *Phys. Rev. Lett.* **1996**, *77*, 3865–3868.

[29] S. Grimme, J. Antony, S. Ehrlich, H. Krieg, *J. Chem. Phys.* **2010**, *132*, 154104.

[30] M. J. Frisch, G. W. Trucks, H. B. Schlegel, G. E. Scuseria, M. A. Robb, J. R. Cheeseman, G. Scalmani, V. Barone, G. A. Petersson, H. Nakatsuji, et al., *Gaussian 09 (Gaussian Inc., Wallingford, CT)* **2009**.

[31] W. J. Hehre, K. Ditchfield, J. A. Pople, *J. Chem. Phys.* **1972**, *56*, 2257–2261.

[32] M. M. Francl, W. J. Pietro, W. J. Hehre, J. S. Binkley, M. S. Gordon, D. J. DeFrees, J. A. Pople, *J. Chem. Phys.* **1982**, *77*, 3654–3665.

[33] T. Clark, J. Chandrasekhar, G. W. Spitznagel, P. V. R. Schleyer, *J. Comput. Chem.* **1983**, *4*, 294–301.

[34] M. Álvarez-Moreno, C. de Graaf, N. López, F. Maseras, J. M. Poblet, C. Bo, *J. Chem. Inf. Model.* **2015**, *55*, 95–103.

[35] M. A. Ortuño, *Database,* , DOI: http://doi.org/10.19061/iochem-bd-1-113

[36] B. D'Andrade, S. Datta, S. Forrest, P. Djurovich, E. Polikarpov, M. Thomsom, *Org. Electron.* **2005**, *6*, 11–20.

[37] S. Badgujar, G.-Y. Lee, T. Park, C. E. Song, S. Park, S. Oh, W. S. Shin, S.-J. Moon, J.-C. Lee, S. K. Lee, *Adv. Energy Mater.* **2016**, *6*, 1600228.

[38] A. J. Knight, A. D. Wright, J. B. Patel, D. P. McMeekin, H. J. Snaith, M. B. Johnston, L. M. Herz, *ACS Energy Lett.* **2018**, 75–84.

[39] X. Wen, Y. Feng, S. Huang, F. Huang, Y.-B. Cheng, M. Green, A. Ho-Baillie, *J. Mater. Chem. C* **2016**, *4*, 793.

[40] Y. Yamada, T. Yamada, A. Shimazaki, A. Wakamiya, Y. Kanemitsu, *J. Phys. Chem. Lett.* **2016**, *7*, 1972–1977.

[41] J. Kim, R. Godin, S. D. Dimitrov, T. Du, D. Bryant, M. A. McLachlan, J. R. Durrant, *Adv. Energy Mater.* **2018**, *1802474*, 1802474.

[42] H. J. Snaith, A. Abate, J. M. Ball, G. E. Eperon, T. Leijtens, N. K. Noel, S. D. Stranks, J. T.-W. Wang, K. Wojciechowski, W. Zhang, *J. Phys. Chem. Lett.* **2014**, *5*, 1511–1515.

[43] D. A. Jacobs, Y. Wu, H. Shen, C. Barugkin, F. J. Beck, T. P. White, K. Weber, K. R. Catchpole, *Phys. Chem. Chem. Phys.* **2017**, *19*, 3094–3103.

[44] A. Pockett, M. J. Carnie, *ACS Energy Lett.* **2017**, *2*, 1683–1689.

[45] P. Calado, A. M. Telford, D. Bryant, X. Li, J. Nelson, B. C. O'Regan, P. R. F. F. Barnes, *Nat. Commun.* **2016**, *7*, 13831.

[46] P. Schilinsky, C. Waldauf, C. J. Brabec, *Appl. Phys. Lett.* **2002**, *81*, 3885–3887.

[47] I. Riedel, J. Parisi, V. Dyakonov, L. Lutsen, D. Vanderzande, J. C. Hummelen, *Adv. Funct. Mater.* **2004**, *14*, 38–44.

Table of contents

Supramolecular Coordination of Pb^{2+} Defects in Hybrid Lead Halide Perovskite Films Using Truxene Derivatives as Lewis Base Interlayers.

Ece Aktas, Jesús Jiménez-López, Cristina Rodríguez- Seco, Dr. Rajesh Pudi, Dr. Manuel A. Ortuño, Prof. Núria López, and Prof. Emilio Palomares*

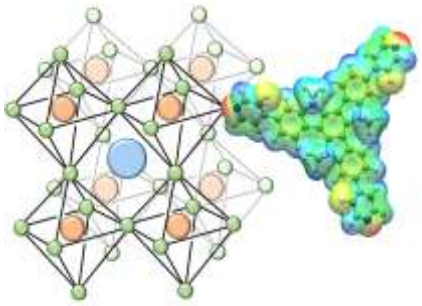

In this work, we synthesized a pyridine functionalized truxene core that is able to form a Lewis acid/Lewis base supramolecular interaction (see picture). This small molecule works as a passivation layer on top of the perovskite thin film, reducing carrier recombination in perovskite solar cells.